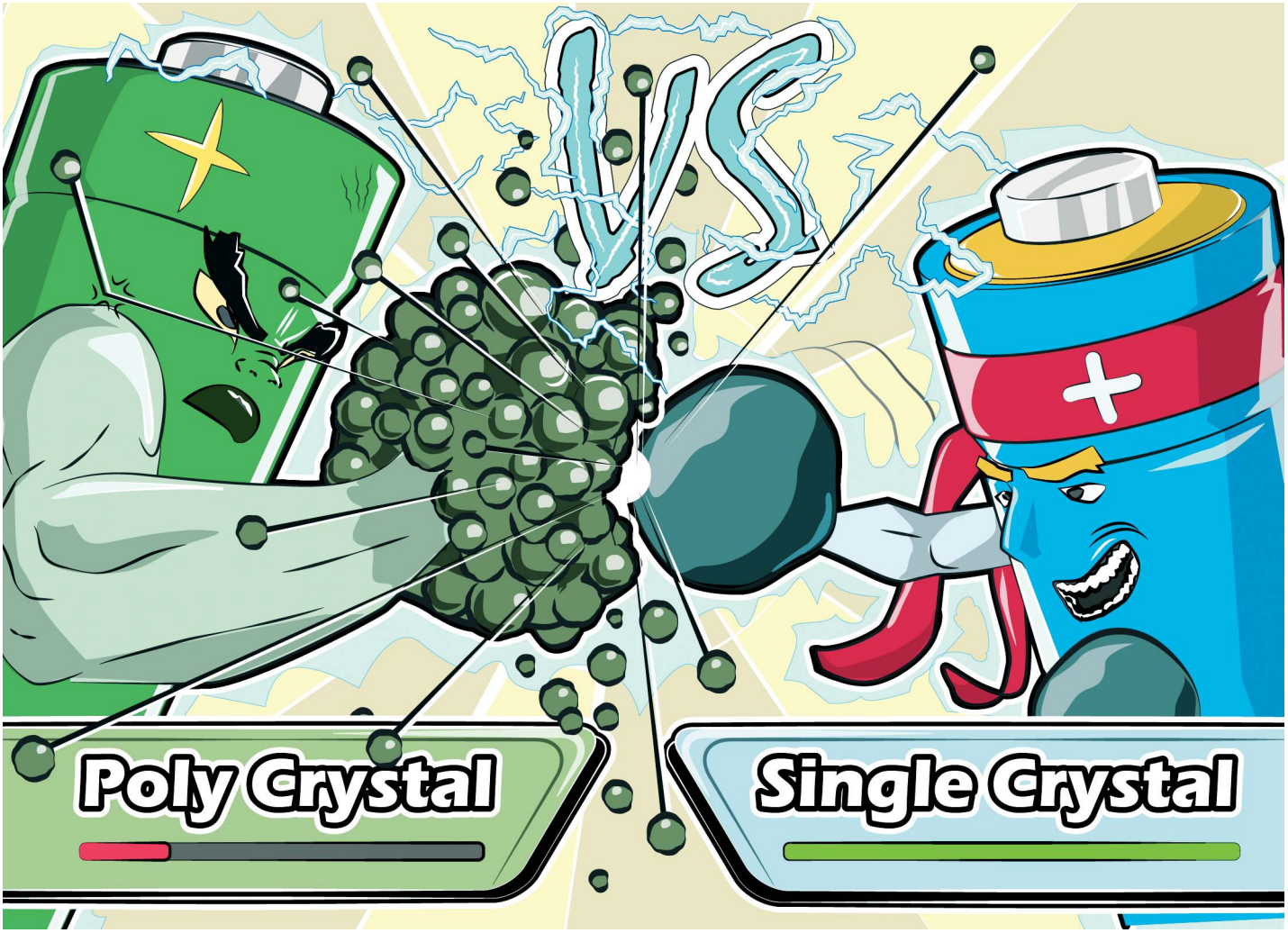

Highlighting a study on "Prospects and Limitations of Single-Crystal Cathode Materials to Overcome Cross-Talk Phenomena in High-Voltage Lithium Ion Cells" by a group of researchers led by Sven Klein and Dr Tobias Placke from Münster Electrochemical Energy Technology and Prof. Martin Winter and Dr Johannes Kasnatscheew from Jülich Research Centre.

Prospects and limitations of single-crystal cathode materials to overcome cross-talk phenomena in high-voltage lithium ion cells

Single crystals as a novel particle shape for cathode materials are critically compared with conventional poly crystals. Though, with slight lower initial power, the single crystals remain stable and enhance the cycle life of batteries at high voltage.

As featured in:

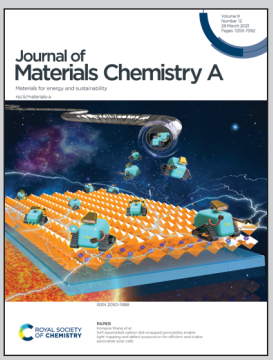

See Martin Winter, Tobias Placke, Johannes Kasnatscheew *et al.*, *J. Mater. Chem. A*, 2021, **9**, 7546.

ROYAL SOCIETY OF CHEMISTRY

rsc.li/materials-a

Registered charity number: 207890

Journal of Materials Chemistry A

ROYAL SOCIETY OF CHEMISTRY

PAPER

View Article Online
View Journal | View Issue

Check for updates

Cite this: *J. Mater. Chem. A*, 2021, **9**, 7546

Prospects and limitations of single-crystal cathode materials to overcome cross-talk phenomena in high-voltage lithium ion cells

Sven Klein,[a] Peer Bärmann,[a] Olga Fromm,[a] Kristina Borzutzki,[b] Jakub Reiter,[cd] Quan Fan,[e] Martin Winter, *[ab] Tobias Placke *[a] and Johannes Kasnatscheew *[b]

Received 3rd December 2020
Accepted 16th February 2021

DOI: 10.1039/d0ta11775g

rsc.li/materials-a

The specific energy of lithium ion batteries can be further enhanced by increasing the cell voltage (>4.3 V). However, conventional cathode active materials (CAMs) *e.g.* $LiNi_{0.5}Co_{0.2}Mn_{0.3}O_2$ (NCM523) with typical poly-crystal (PC)-based secondary particles suffer from rollover failure at 4.5 V, which is shown to be the result of an electrode cross-talk, *i.e.*, dissolution of transition metals (TMs) from the cathode and deposition at the graphite-based anode. Interestingly, the TM deposits at the anode are locally accumulated and dendritic Li deposits are analytically indicated on exactly these spots. Severe formation of Li dendrites is concluded to be the onset of sudden and abrupt capacity fade as it is accompanied by severe consumption of active Li. In contrast, NCM523 CAMs based on single-crystals (SCs), which are single-standing primary particles, demonstrate an improved cycle life in SC-NCM523||graphite cells. Less rollover fading, cross-talk and Li dendrites at the anode are observed and attributed to the morphology of the SC-based cathode. It is concluded that the lower specific surface area diminishes electrolyte contact, thus the reaction area for transition metal dissolution and finally improves the high voltage performance.

Introduction

Enhancing the operation potential of positive electrodes (cathodes) is a common strategy to increase the cell voltage, and thus specific energy and power of batteries.[1–3] State-of-the-art cathode active materials (CAMs) for lithium ion batteries (LIBs) are layered oxides with the typical composition of $LiNi_xCo_yMn_zO_2$ (NCM*xyz*; $x + y + z = 1$), *e.g.*, $LiNi_{0.5}Co_{0.2}Mn_{0.3}O_2$ (NCM523).[4–8]

It is of particular interest to further enhance the charge potential of NCM cathodes above the common limit of 4.3 V *vs.* $Li|Li^+$ and thus the overall cell operation voltage. This comes with a further increase in specific capacity, which additionally boosts the specific energy.[9,10] However, this approach is accompanied by structural instabilities of the NCM materials, followed by parasitic decomposition reactions and severe capacity fading.[9,11,12] Above the potential of 4.3 V *vs.* $Li|Li^+$, a thermodynamically driven decomposition converts the structure of layered oxides to spinel phases and finally to a thermodynamically more stable, but inactive, rock-salt phase.[13,14] These phase changes are intertwined with detrimental oxygen release and transition metal dissolution (*i.e.*, Co, Ni and Mn) into the electrolyte.[15–18] Though, only in marginal amounts relative to NCM,[11,19] the dissolved transition metals can deposit at graphite-based negative electrodes (anodes) and deteriorate the solid electrolyte interphase (SEI)[20–23] in the course of the well-known electrode or electro-(chemical) cross-talk.[15,24–32] As a consequence, this triggers losses of active Li *via* formation of high surface area lithium (HSAL), *e.g.* in the morphological form of dendrites and further decreases the cycle life of LIBs.[15,24] In a previous publication it is shown that this can lead to rollover failure in NCM523||graphite cells.[33]

In addition, also the macroscopic instability of NCM can additionally promote detrimental cross-talk. In general, NCM materials are based on micron-sized secondary particles, which are aggregated by numerous nano-sized primary particles.[34–36] It is known in the literature that secondary particles can crack, in particular promoted by the strain at high voltage operation ("electrochemical shock").[34,37] The increased surface area accompanied by increased exposure to the electrolyte can further promote transition metal (TM) dissolution.[14,38,39] These secondary particles, being prone to inter-granular cracking, are denoted as 'poly-crystal (PC)'-based active materials.[14,34]

[a]*MEET Battery Research Center, Institute of Physical Chemistry, University of Münster, Corrensstraße 46, 48149 Münster, Germany. E-mail: tobias.placke@uni-muenster.de; m.winter@fz-juelich.de*

[b]*Helmholtz-Institute Münster, IEK-12, Forschungszentrum Jülich GmbH, Corrensstraße 46, 48149 Münster, Germany. E-mail: j.kasnatscheew@fz-juelich.de*

[c]*BMW Group, Petuelring 130, 80788 Munich, Germany*

[d]*Inobat Auto, Mostova 6, 811 02 Bratislava, Slovakia*

[e]*Contemporary Amperex Technology Limited, No. 1 XinGang Road, Jiaocheng District, Ningde 352100, Fujian Province, China*

A smart approach to circumvent inter-granular cracking and to minimize the overall surface area of CAMs is the use of non-agglomerated, thus single, primary particles with an enhanced particle size ($\approx$5 μm).[40,41] These are denoted in the literature as 'single-crystal (SC)' with reported superior performance for various SC-based CAMs, including NCM523, NCM622 and NCM811.[42–48] Moreover, in line with calculations from fracture mechanics, larger primary particles are supposed to be mechanically more stable in regard to intra-granular cracking compared to smaller particles.[14,49,50] This overall mechanical stability is beneficial also in terms of electrode processing as it renders them less prone to cracking, *e.g.* during pressing, and can realize higher electrode densities, and thus higher areal capacities.[14,51]

In this work, the behavior of a SC-NCM523-based CAM is thoroughly investigated in a NCM523‖graphite full-cell under high voltage conditions (upper cell voltage: 4.4 V to 4.7 V) in contrast to conventional PC-NCM523. Significant performance differences due to appropriate morphological alteration are highlighted and discussed with the support of electrochemical and analytical methods.

Experimental

Electrode preparation

NCM523-based cathodes (PC- and SC-CAMs purchased from Umicore and CATL, respectively) and graphite-based anodes were prepared in large-scale at an in-house battery line. The cathodes consisted of 95 wt% NCM523 (pristine NCM523; Custom Cells Itzehoe GmbH), 3 wt% polyvinylidene fluoride (PVdF) binder (Solef 5130, Solvay) and 2 wt% carbon black (Super C65, Imerys Graphite & Carbon) and were cast onto aluminum foil (15 μm; Nippon Foil). The used solvent was *N*-methyl-2-pyrrolidone (NMP, Sigma Aldrich, purity: 99.5%). The mass loadings for the SC-NCM523-based cathodes and the PC-NCM523-based cathodes were 8.7 mg cm^{-2} and 10.6 mg cm^{-2}, respectively. The anodes consisted of 95 wt% graphite (SG3, synthetic graphite, SGL Carbon), 1.5 wt% styrene-butadiene-rubber (SBR; SB5521, LIPATON, Polymer Latex GmbH), 3 wt% Na-CMC (Walocel CRT 2000 PPA12; Dow Wolff Cellulosics) and 0.5 wt% carbon black (Super C65, Imerys Graphite & Carbon) and were cast onto copper foil (10 μm; Nippon Foil). The used solvent was deionized water. Two different mass loadings were prepared for the anodes, *i.e.*, (a) 8.5 mg cm^{-2} and (b) 6.8 mg cm^{-2}. After drying and calendaring of the electrode sheets, the electrodes were punched into circular Φ14 mm (cathode) and Φ15 mm (anode) discs. The electrodes were dried in a vacuum oven at 100 °C under reduced pressure.

Cell assembly

2032-type coin cells (two-electrode configuration)[52] were assembled to investigate TM dissolution from the NCM523 cathode and TM deposition at the graphite anode in NCM523‖graphite full-cells. The Φ15 mm anode disc was separated by a Celgard 2500 separator (polypropylene, one layer) from the Φ14 mm cathode disc, which was soaked with 40 μL electrolyte (1 M $LiPF_6$ in EC/EMC 3 : 7 by weight, Solvionic; purity: battery grade).

Constant current-constant voltage charge/discharge cycling

The electrochemical charge/discharge cycling performance of NCM523‖graphite full-cells was studied *via* constant current (CC) charge/discharge cycling on a Maccor 4000 battery testing system in cell voltage ranges from (a) 2.8–4.3 V, (b) 2.8–4.4 V, (c) 2.8–4.5 V, (d) 2.8–4.6 V and (e) 2.8–4.7 V. The cell formation conditions consisted of one cycle at 0.1C and one cycle at 0.2C within the respective cell voltage range. Afterwards, the cells were cycled at 1C (1C = 210 mA g^{-1} at 4.7 V; 1C = 200 mA g^{-1} at 4.6 V, 1C = 190 mA g^{-1} at 4.5 V, 1C = 180 mA g^{-1} at 4.4 V, 1C = 170 mA g^{-1} at 4.3 V). After each charge step, a constant voltage (CV) step was performed with the limiting conditions of either achieving a time limit of maximum 30 minutes or when the specific current reaches values below 0.05C. All electrochemical studies were performed in climatic chambers at 20 °C. At least three cells were evaluated for each study in order to ensure high reproducibility, which is indicated by error bars in the respective figures.

SEM and EDX investigations

The surface morphology of the cycled graphite anodes was investigated using a Zeiss Auriga electron microscope and EDX was carried out with an accelerating voltage of 20 kV with an energy-dispersive X-ray detector (X-MaxN 80 mm^2, Oxford Instruments). Prior to analysis, the cells were disassembled in a dry atmosphere (dry room) and the anode surfaces were rinsed with 1 mL EMC. After a short drying period under reduced pressure, the electrodes were transferred into the SEM device *via* a vacuum sealed sample holder to avoid any contact with moisture.

BET specific surface area and PSA investigations

A 3Flex Physisorption surface analyzer (Micromeritics GmbH) was used to determine the specific surface area of the anodes at a temperature of −196 °C by applying the Brunauer–Emmett–Teller (BET) model.[53,54] Prior to the measurements, the anodes were degassed for at least 12 h at 100 °C (80 × Φ15 mm electrodes). Particle size distributions were measured with a Cilas 1064 Particle Size Analyzer (PSA). Prior to measurements, the samples were dispersed in water with the help of a detergent.[55]

Results and discussion

Charge/discharge cycling in NCM523‖graphite cells: kinetic differences

The visual comparison of poly- *vs.* single-crystal $LiNi_{0.5}Co_{0.2}Mn_{0.3}O_2$ electrodes (PC-NCM523 *vs.* SC-NCM523) *via* scanning electron microscopy (SEM) is depicted in Fig. 1. The conventional PC-NCM523 (Fig. 1(a)) appears as a micron-sized secondary particle (D_{90} = 13.9 μm) based on agglomerated nano-sized primary particles. In contrast, SC-NCM523 solely consists of significantly larger but single-standing primary

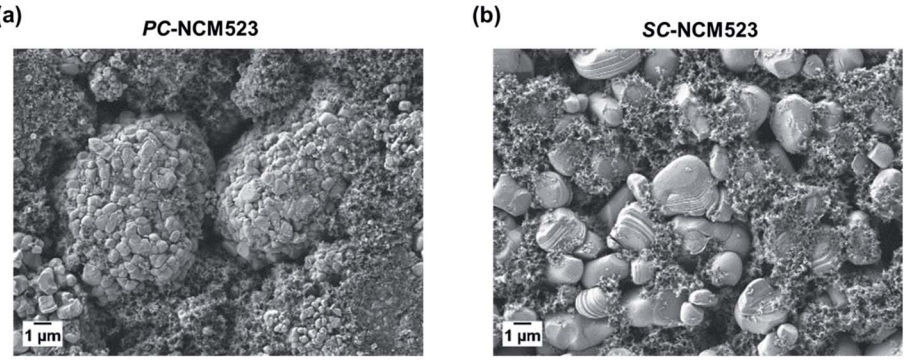

Fig. 1 SEM images of the cathodes based on (a) PC-NCM523 and (b) SC-NCM523 with D_{90} values of 13.9 and 7.0 µm and BET surface areas of 1.62 and 0.99 $m^2\ g^{-1}$, respectively.

particles only ($D_{90} = 7.0$ µm). The SC-morphology has finally an overall lower BET surface area (0.99 $m^2\ g^{-1}$) compared to PC-NCM523 (1.62 $m^2\ g^{-1}$).

The first charge/discharge cycles of PC- and SC-NCM523||graphite full-cells are depicted in Fig. 2 for the varied charge cut-off cell voltages of 4.3 V, 4.4 V and 4.5 V. Characteristic of NCM, the specific capacity increases with increasing the charge cut-off cell voltage. Independent of the applied cut-off cell voltage, the specific capacity losses remain nearly unaffected for each electrode, which hints at the stability of both the active and inactive materials.[13,56]

The total specific capacity losses differ for each material, and are 25 mA h g^{-1} and 32 mA h g^{-1} for PC-NCM523 and SC-NCM523, respectively. As the apparent specific capacity losses of NCMs are overwhelmingly the result of a kinetically reasoned incomplete lithiation, the different specific capacity losses point to kinetic differences of the two materials, likely due to longer Li^+ transport within the larger primary particle size of SC-NCM523.[57]

Differences in kinetics emerge more clearly for processes that additionally hamper the Li^+ transport within NCM, *e.g.* after structural decomposition. In this regard, both NCM523 cells are overcharged up to 4.7 V and the voltage profiles are depicted in Fig. 3(a). Structural changes can be concluded from the increased specific capacity losses towards 33.5 mA h g^{-1} and 39.3 mA h g^{-1} for the PC- and SC-NCM523-based cells, respectively, compared to cells cycled under milder conditions. Despite the low rate (0.1C) already significant differences in voltage drop can be observed, which are 0.05 V and 0.14 V for PC- and SC-NCM523-based full-cells, respectively. For higher rates, the kinetic differences are even more evident, *e.g.* 0.1C *vs.* 1.0C, as depicted in Fig. 3(b). Here, in addition to the increased voltage-drop (0.08 V and 0.20 V for PC- and SC-NCM523-based full-cells) at the end of charge/beginning of discharge, the overvoltage increases in general, and thus the overall voltage hysteresis is larger; both being suitable indicators for poorer kinetics.[56,57] According to the literature, changes in size and morphology of cathode active material particles significantly impact the kinetic aspects *via* changes in the Li^+ transport length within the active material, while possible changes in electron conductivity can be regarded as less relevant as long as

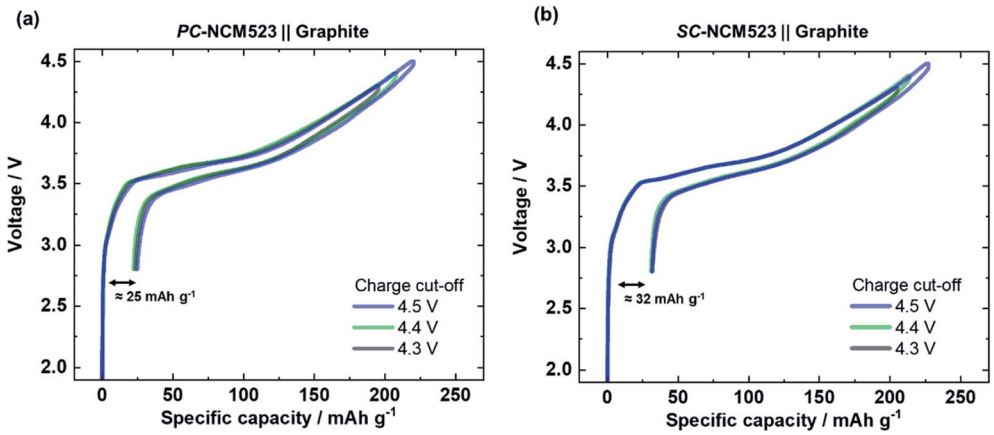

Fig. 2 The 1st charge/discharge cell voltage profiles of NCM523||graphite full-cells as a function of specific capacity at three different charge cut-off cell voltages and a rate of 0.1C for cells based on the (a) PC-NCM523 and (b) SC-NCM523 materials. The specific capacity loss does not increase with increasing cut-off cell voltage for each cell, thus, pointing to initial stability of the materials. The difference in specific capacity loss between the cells (25 *vs.* 32 mA h g^{-1}) hints at kinetic differences between the PC-NCM523 and SC-NCM523 materials, likely associated with different sizes of primary particles.

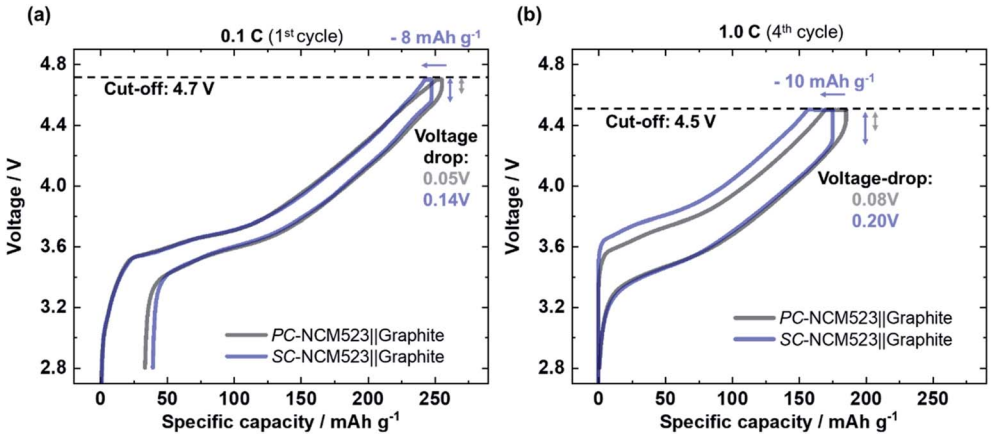

Fig. 3 (a) Cell voltage profiles of NCM523||graphite full-cells as a function of specific capacity of the 1st charge discharge cycle with a cut-off voltage of 4.7 V (0.1C). Differences in the profiles of PC-NCM523 and SC-NCM523 evolve above 4.5 V, leading to differences in voltage-drop despite the low rate. (b) Cell voltage profiles of the 4th charge/discharge cycle with a cut-off voltage of 4.5 V and an increased rate of 1.0C. Given the poorer kinetics, SC-NCM523 has lower specific capacities than PC-NCM523.

a sufficient conductive agent (*e.g.* carbon black) is embedded within the cathode composite.[57]

Cycle life of NCM523||graphite cells and analysis of graphite anodes

The specific discharge capacities during continuous charge/discharge cycling for the varied charge cut-off cell voltages of 4.3 V, 4.4 V and 4.5 V are depicted in Fig. 4. Despite slightly higher initial specific discharge capacities of the PC-NCM523-based cells (Fig. 4(a)), at 4.5 V both cells reveal a sudden and severe capacity fading after ≈70 cycles, also known as rollover failure,[58] while the SC-NCM523-based cells (Fig. 4(b)) reveal a significantly improved capacity retention at 4.5 V without this failure. The rollover failure observed for the PC-NCM523||graphite cells frequently appears for high-voltage LIB applications.[30,31,58–61] The abrupt nature of this fading type and its dependence on the type of anode (typical for graphite) point to a cross-talk between the electrodes. Interacting processes, where both electrodes are involved can be for example a cross-over of dissolved TMs, *i.e.* Ni, Co and Mn from the cathode to the anode and/or a short-circuit *via* penetrating high surface area Li (HSAL), *e.g.*, Li metal dendrites from the anode to cathode.

Penetration of Li metal dendrites through the separator/electrolyte is particularly investigated in Li metal batteries (LMBs).[62–65] Li dendrites are formed and grow during charge, and thus can significantly increase the specific charge capacities *via* short-circuits in case of penetration.[63,64] To validate this possibility, the specific charge capacities during charge/discharge cycling for 4.5 V are examined and depicted in Fig. 5(a) for both cells. Indeed, after the onset of the rollover cell failure of the PC-NCM523||graphite cells after ≈70 cycles, the specific charge capacities significantly increase and have fluctuating values. The evolved total irreversible capacities, as a difference between charge and discharge, are too high to intrinsically originate from the NCM itself. Instead, the high

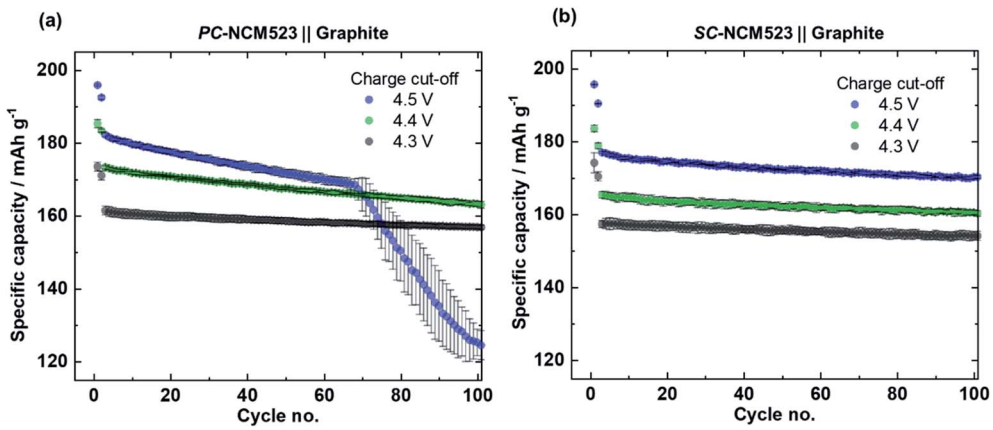

Fig. 4 Specific discharge capacities as a function of cycle number of (a) PC-NCM523||graphite and (b) SC-NCM523||graphite full-cells with varied charge cut-off cell voltages of 4.3 V, 4.4 V and 4.5 V. After 70 cycles, the PC-NCM523-based cells encounter a rollover failure when the charge cut-off is 4.5 V.

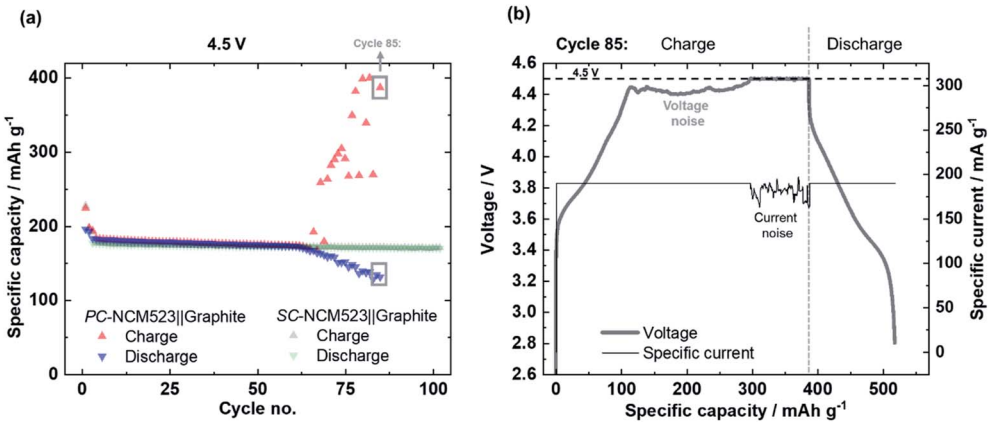

Fig. 5 (a) Specific charge capacities as a function of cycle number of the PC- and SC-NCM523||graphite full-cells for a charge cut-off cell voltage of 4.5 V. During rollover cell failure, the PC-NCM523-based cells reveal saliently random and high specific charge capacities, *e.g.* cycle in no. 85. (b) Cell voltage- and specific current profile as a function of specific capacity for cycle no. 85. The increased specific charge capacity can be related to a cell voltage and specific current noise during galvanostatic charge and the constant voltage step at 4.5 V, respectively, hinting at the penetration of Li metal dendrites through the separator.

and random values rather originate from the sudden appearance of parasitic side reactions, *e.g.*, from (micro-) short-circuits between the anode and cathode. A deeper look at the profiles of the cell voltage and specific current within an exemplary "failure cycle" (no. 85) validates this proposition, which is shown in Fig. 5(b). Both the profiles suffer from cell voltage- and current-noise during constant current- and constant potential (CP)-charge, respectively. Such noisy electrochemical responses are known as valid indicators for micro-short circuits in LMBs,[63,64,66] and apparently point to Li dendrite penetration even in PC-NCM523-based cells. This noise can be attributed to a competitive reaction between conventional NCM delithiation and undesired lithiation *via* the micro short-circuits, finally resulting in the characteristic random up and down in the cell voltage or current, respectively.

To alternatively prove the presence of Li metal dendrites, aged graphite-based electrodes (after 100 cycles) are visualized with SEM under inert conditions and depicted in Fig. 6. In fact, salient deposits can be seen at the graphite surface from PC-NCM523-based cells (Fig. 6(a)), contrary to the graphite surface from SC-NCM523-based cells (Fig. 6(b)). Energy dispersive X-ray (EDX) analysis of this area demonstrates strong F signals at exactly the spots of the deposits, despite previous washing of the electrodes. This may hint at deposited decomposition products of the electrolyte salt, at the reactive Li deposits. Additional insights and evidence for the attribution of these deposits to Li dendrites, including thorough analytical investigations (*e.g.* Li NMR), are elaborated in our previous work.[33]

The presence of Li metal dendrites at the anode for the PC-, but not the SC-NCM523-based cathodes can be reasonably related to a cross-talk of the electrodes, *i.e.* dissolution of the

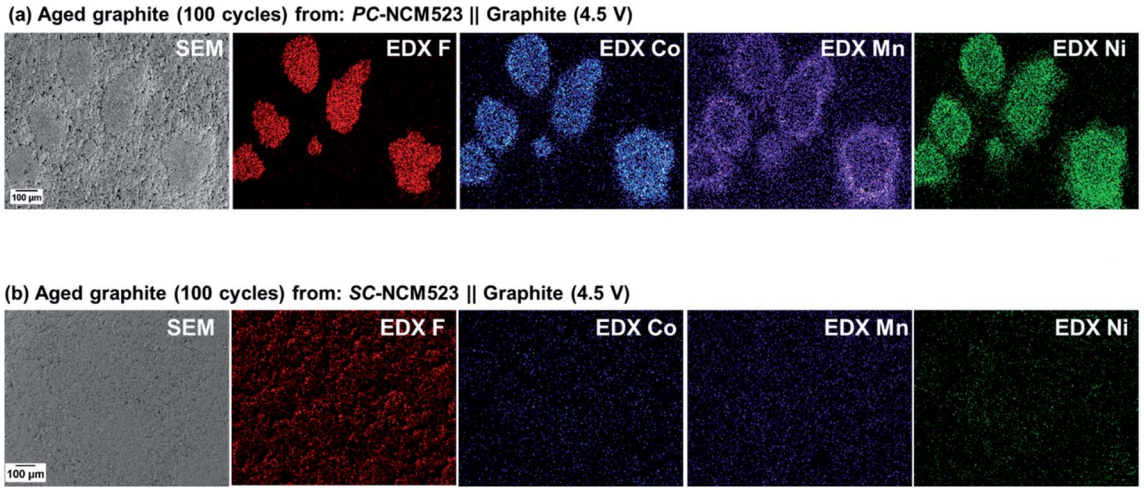

Fig. 6 SEM and SEM-EDX images of cycled (aged) graphite from the (a) PC-NCM523||graphite full-cells and (b) SC-NCM523||graphite full-cells after 100 cycles at 4.5 V charge cut-off cell voltage. Graphite from PC-NCM523 reveals Li metal dendrites at the surface with accumulated transition metals, *i.e.* Co, Mn and Ni at exactly the same spots as the Li dendrites.

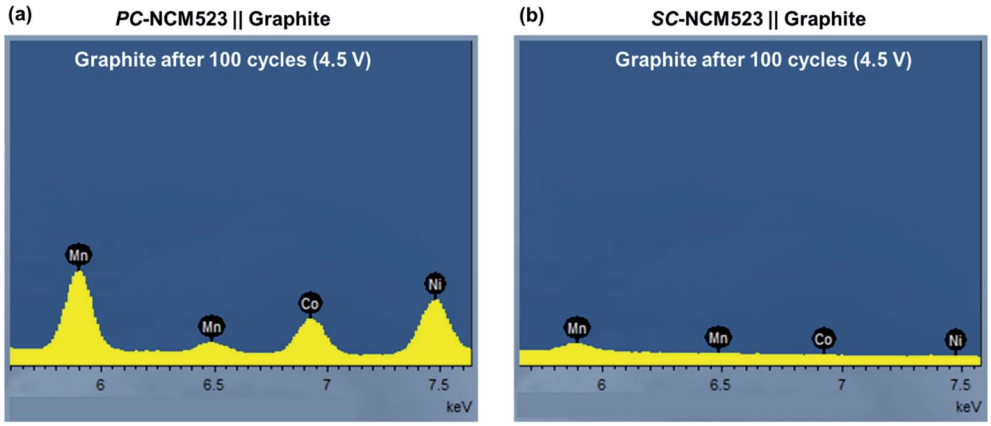

Fig. 7 EDX obtained intensity of Ni, Co and Mn on aged graphite from the (a) PC-NCM523- and (b) SC-NCM523-based cells after 100 cycles with 4.5 V charge cut-off.

transition metals from NCM523 and deposition on graphite. Indeed, based on visualization and elemental detection *via* SEM-EDX for Co, Mn and Ni, this relation can be experimentally concluded. As seen in Fig. 6(a), the transition metals are accumulated and located at identical spots to the Li metal dendrites. In contrast, no spots of transition metals at the graphite surface

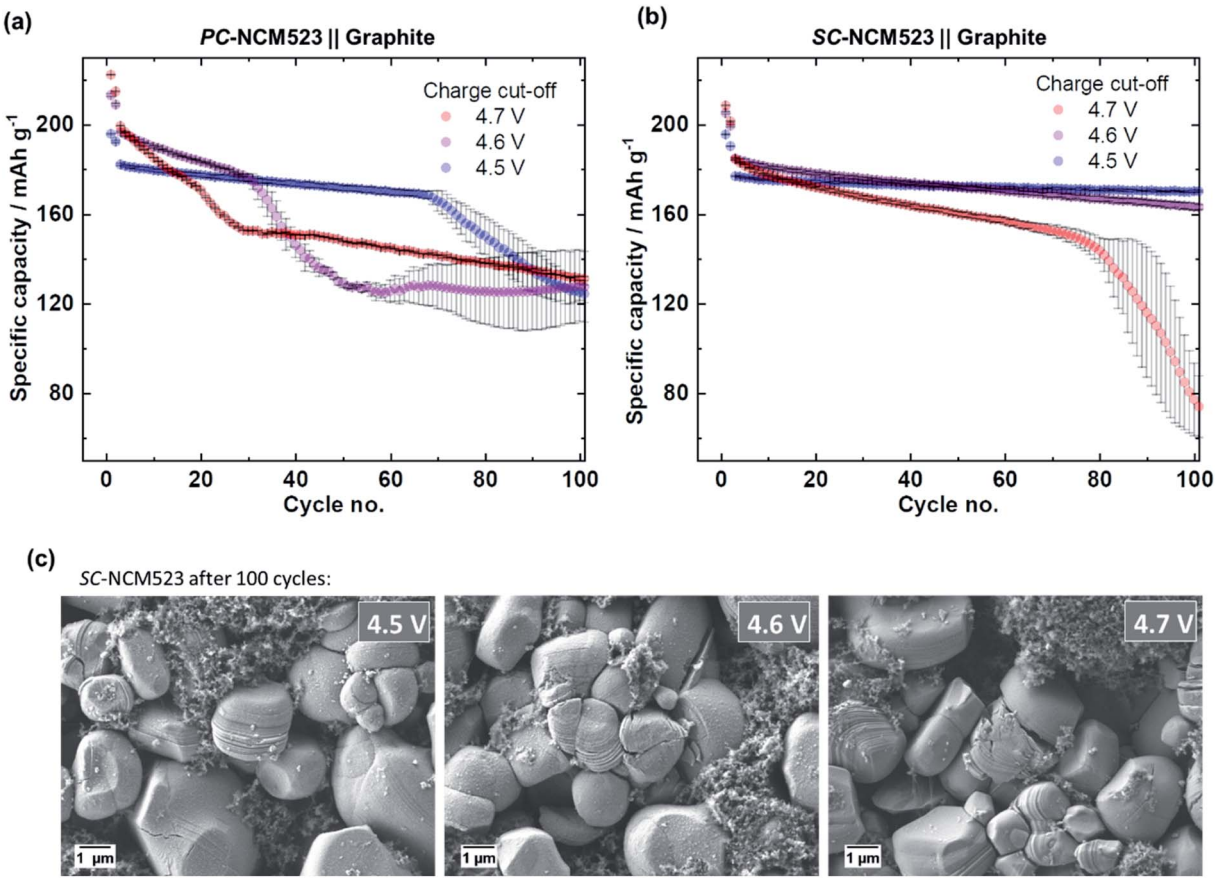

Fig. 8 Specific discharge capacities of NCM523||graphite full-cells as a function of cycle number of (a) PC-NCM523- and (b) SC-NCM523-based cells with varied charge cut-off voltages of 4.5 V, 4.6 V and 4.7 V. With increasing cut-off cell voltage, the capacity fade begins at lower cycle numbers for the PC-NCM523-based cells but without characteristic rollover behavior. For the SC-NCM523-based cells, the rollover is only obtained at the highest shown voltage of 4.7 V. (c) SEM images of SC-NCM523 after 100 cycles at 4.5 V, 4.6 V and 4.7 V. SC-NCM523 begins progressively to crack slightly above 4.6 V, which also demonstrates its mechanical instability, though to a low extent and only at a very high cell voltage.

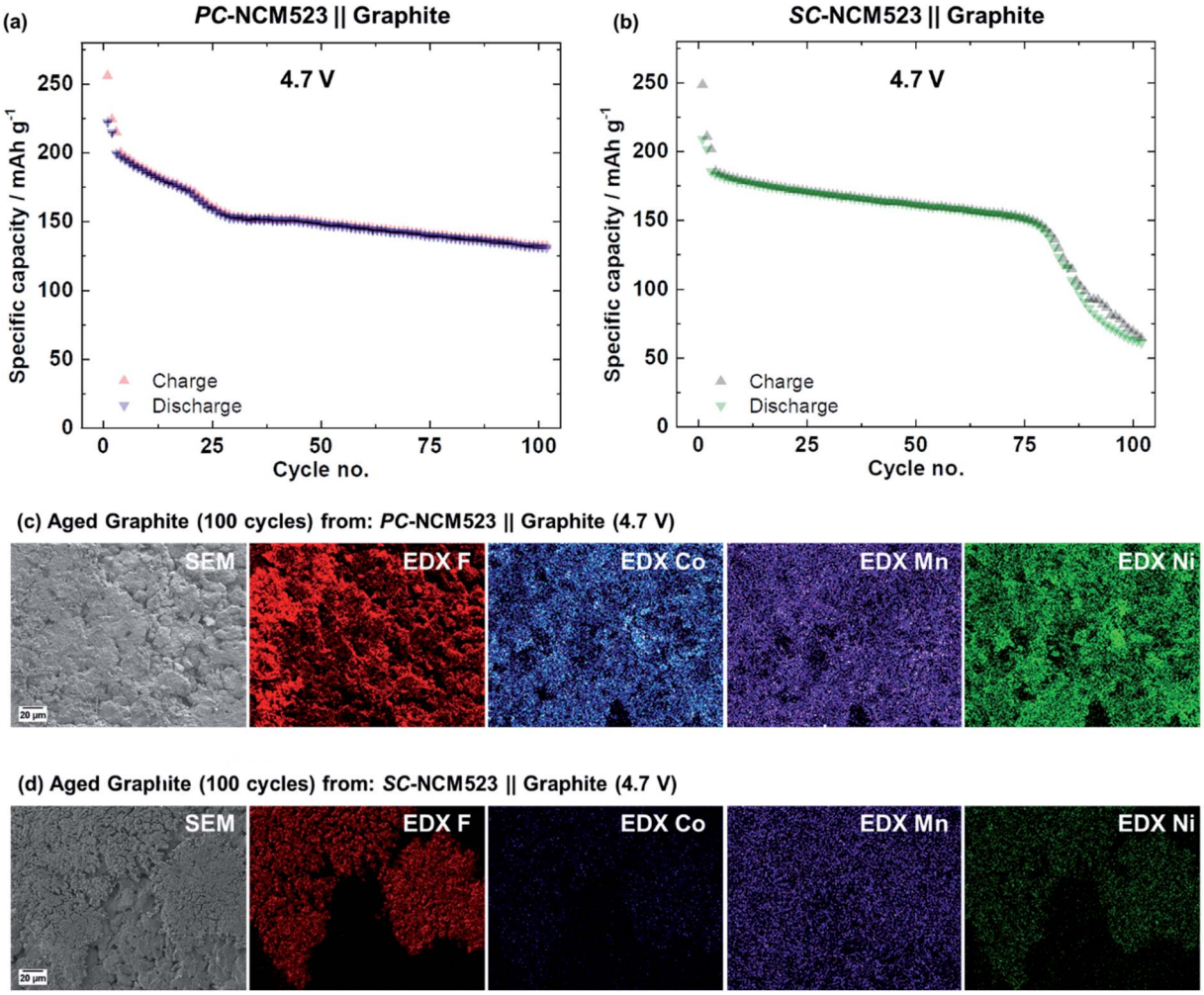

Fig. 9 Specific capacities for charge and discharge at 4.7 V for (a) PC-NCM523- and (b) SC-NCM523-based cells. SEM-EDX images of aged graphite after 100 cycles from (c) PC-NCM523- and (d) SC-NCM523-based cells.

are observed for SC-NCM523. Thus, the presence of Li metal dendrites is likely related to accumulated depositions of transition metals, rendering the transition metal dissolution/deposition the significant difference in terms of rollover cell failure between the PC- and SC-NCM523-based cells.[67]

EDX-obtained intensities of the transition metals at the graphite surface are depicted in Fig. 7. The significantly higher intensities for PC-NCM523-based cells (Fig. 7(a)) compared to those for SC-NCM523-based cells (Fig. 7(b)) clearly confirm the greater transition metal dissolution of the PC-NCM523-based active materials. Their lower primary particle size combined with inter-granular instability of the secondary particles lead to a high and progressively increasing surface area of PC-NCM523 during charge/discharge cycling, respectively. More exposure to the wetting electrolyte obviously leads to more transition metal dissolution compared to SC-NCM523. This method allows a direct comparison of the degree of TM depositions, which supports the evaluation. A more thorough analytical comparison in a quantitative manner, *e.g. via* ICP-OES, is methodically challenging and beyond the scope of this work, as the sticky nature of the cathode and anode (particularly the TM contaminated Li dendrites) towards the separator renders precise measurements not possible for these purposes, while EDX mapping can simply provide the required comparison.

An appropriate morphological difference of the CAM affects the overall cross-talk within the cell *via* a lower amount of dissolved/deposited transition metals. The rollover failure can be regarded as the onset, where Li dendrites are formed on the transition metal enriched graphite surface. The surface of metallic Li in the form of *e.g.* Li dendrites readily reacts with the electrolyte, finally leading to a rapid decrease of active Li, and thus the overall specific cell capacity.

Behavior at very high voltages (up to 4.7 V)

Moving from PC-NCM523- to SC-NCM523-based CAMs improves the cycle life and prevents rollover cell failure at voltages up to 4.5 V. Given electrode cross-talk as the origin of failure, the rollover can also be expected to proceed in SC-NCM523||graphite full-cells, *e.g.*, when dissolution is additionally triggered by further enhancing the voltage above 4.5 V. To prove this relation, the charge cut-off voltages are further

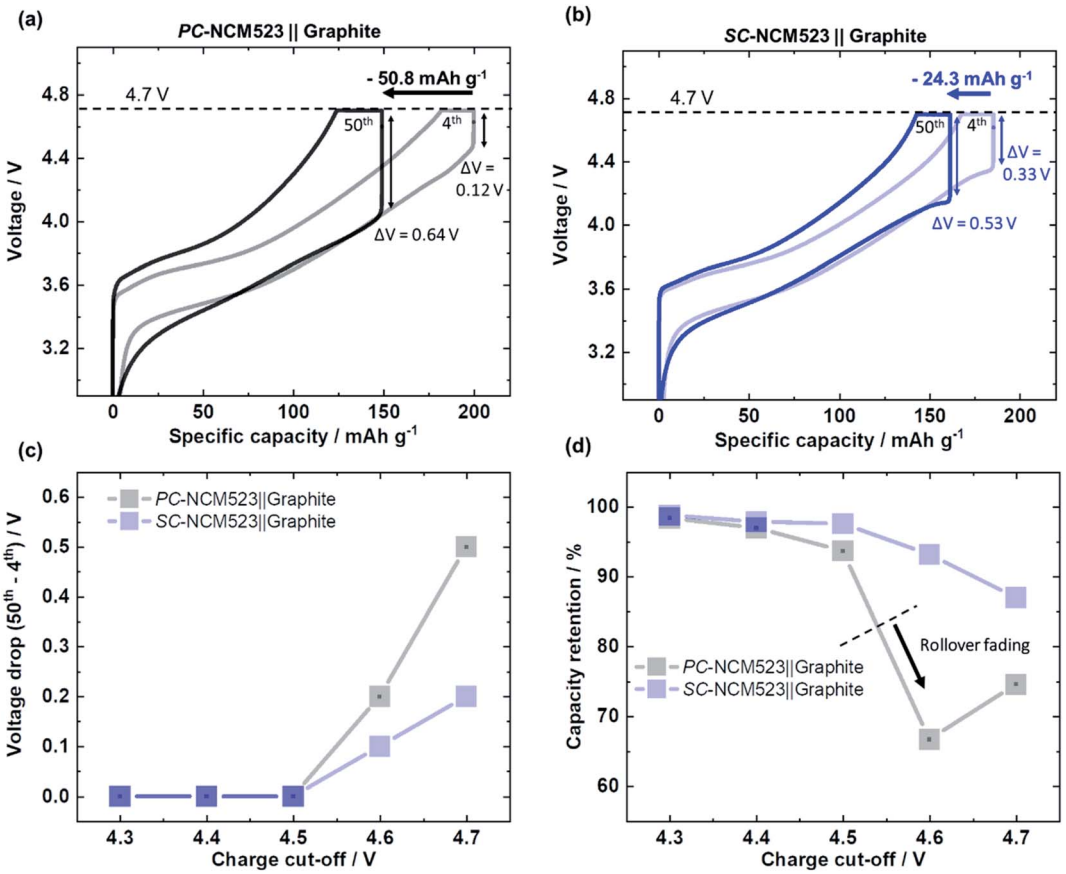

Fig. 10 4th and 50th charge discharge cycles at 1.0C of the (a) PC-NCM523- and (b) SC-NCM523-based cells. (c) The increase in voltage drop as a difference between the 50th and 4th cycle and (d) the capacity retention (50th *vs.* 4th cycle) as a function of charge cut-off voltage. Data point to a significantly improved cycle life behavior, and thus to an additional application relevant advantage of SC-NCM523.

enhanced towards 4.6 V and 4.7 V and the specific discharge capacities are depicted in Fig. 8.

It is shown that the fading of the PC-NCM523-based cells above 4.5 V is more severe and begins at significantly lower cycle numbers (Fig. 8(a)). Interestingly, the fading at 4.7 V cannot be attributed to the characteristic rollover failure, as the decay in specific capacity is continuous from the beginning on and is highly reproducible, as seen by the low error bars. Also, no characteristic increase in specific charge capacities can be observed relative to the specific discharge capacities as shown in Fig. 9(a). Finally, the SEM-EDX images of aged graphite, displayed in Fig. 9(c), show an intense, but homogeneous distribution of F- and TMs, instead of the rollover-characteristic accumulated spots. It can be concluded that the characteristic rollover failure appears for a distinct range in deposited TM amounts. Although it also results in active Li losses and capacity decay, a too high TM concentration obviously reveals a different HSAL morphology from Li dendrites, a Li deposition morphology which is characteristic for rollover fading.

For SC-based cells, rollover failure can be detected, but only at 4.7 V (Fig. 8(b)). Compared to the rollover failure discussed for the PC-NCM523-based cells at 4.5 V, the rollover failure of the SC-NCM523-based cells is milder in effect and occurs less abruptly. The increased specific charge capacities relative to specific discharge capacities during the sudden failure, shown in Fig. 9(b), also indicate rollover behavior, but again, this is significantly milder compared to that of the PC-NCM523-based cells at 4.5 V. This in line with the SEM-EDX images shown in Fig. 9(d). Characteristic accumulated spots of F-, Co- and Ni can be seen on graphite, but in significantly lower concentrations as observed for the PC-NCM523-based cells at 4.5 V in Fig. 6(a). As shown in Fig. 8(c), SC-NCM523 slightly starts to crack above 4.6 V and can be reasonably related to the rollover fading due to *e.g.* cracking-related increase in surface area. In summary, the SC-NCM523-based materials obviously can also crack and suffer from rollover failure, which finally proves the principle. However, this happens to a significantly less extent and at significantly higher voltages compared to PC-NCM52. A thorough further differentiation and analysis of capacity fading is part of our next work and can be evaluated *e.g.* by exchanging graphite with a Li metal anode, and thus by investigating in a system where active Li is not limited, which can allow distinguishing of failure due to cross-talk or the cathode itself.

Obviously, the SC-NCM523-based cells are beneficial with respect to cycle life at high voltages as they minimize the electrode cross-talk, and thus the risk for rollover fading and an abrupt end of life. Besides the electrode cross-talk, which is a chemical aspect, the stable nature of SC-NCM523 also reveals improved cycle life characteristics in an electrochemical manner, which is even more pronounced with increasing

voltage. As seen in Fig. 10(a), the PC-NCM523-based cells suffer from a capacity decay of 50.8 mA h g^{-1} and an increase in voltage drop of 0.52 V at 4.7 V between cycle no. 4 and no. 50. In contrast, the respective decay in capacity for the SC-NCM523 cells is only 24.3 mA h g^{-1}, while the increase in voltage drop is only 0.20 V, as seen in Fig. 10(b). The voltage drop, as an indication of kinetic aspects (relevant for high rate performance, low temperature applications, *etc.*) is initially higher for the SC-NCM523-based cells, but their rise is lower during cycling and after several cycles becomes even lower compared to that of the PC-NCM523-based cells (Fig. 10(b)). In other words, the kinetic aspects of the PC-NCM523-based cells are becoming worse during cycling at higher voltages compared to those of the SC-based cells as shown in Fig. 10(c). Accompanied by this, capacity retention during cycling (the 50^{th} to 4^{th} cycles) is significantly better for the SC-NCM523-based cells compared to that for the PC-NCM523-based cells, *i.e.* also for cycles before the onset of rollover fading, as shown in Fig. 10(d).

Conclusion

Enhancing the cell voltage of lithium ion batteries (LIBs) above 4.3 V remains a significant challenge in terms of sufficient cycle life both at the anode and cathode of the cell system. As shown in this work for conventional $LiNi_{0.5}Co_{0.2}Mn_{0.3}O_2$ (NCM523)‖ graphite cells, a cell voltage increase up to 4.5 V results in rollover cell failure, which is seen as an abrupt and severe capacity decrease during charge/discharge cycling, here at cycle number 80. The noisy profiles of cell voltages and specific currents indicate (micro-) short circuits, likely *via* penetration of Li metal dendrites from the graphite anode through the separator to the cathode. This is experimentally confirmed and visualized on the graphite surface with a scanning electron microscope (SEM). Exactly at the spots of localized Li dendrites, accumulated transition metals (Ni, Co, and Mn) are detected *via* the SEM- energy dispersive X-ray (EDX) technique. Hence, the rollover failure can be concluded to be the result of cross-talk between the cathode and anode *via* cross-over of dissolved transition metals and deposition at graphite. The onset of the rollover failure is intertwined with severe Li dendrite formation and in some cases even penetration, which, given its reactivity results in losses of active Li, and thus decay in specific capacity.

An appropriate morphological change from conventional poly-crystal (PC)-based NCM523 towards single-crystal (SC)-based NCM523 diminishes this failure. SC-based NCM523 as single-standing primary particle has overall a larger particle size and lower specific surface area, thus, rendering less area for electrolyte wetting and subsequent dissolution of transition metals. Given the diminished cross-talk between the electrodes, Li dendrites could not be found on SC-based NCM523. However, rollover fading and slight particle cracking can also be confirmed for this material, but to a significantly less extent and only at a very high cell voltage (4.7 V). These performance data consequently show that a higher cell voltage can be applied for SC-based NCM523-cells, which are thus more reasonable candidates for high voltage applications than PC-based cathode systems.

Conflicts of interest

There is no conflict of interest to declare.

Acknowledgements

The authors of WWU Münster wish to thank the BMW Group and CATL for financial support of this work. Additionally, the authors thank SGL Carbon for material supply.

References

1 J. B. Goodenough and Y. Kim, *J. Power Sources*, 2011, **196**, 6688–6694.
2 J. Kasnatscheew, R. Wagner, M. Winter and I. Cekic-Laskovic, *Top. Curr. Chem.*, 2018, **376**, 16.
3 M. Winter, B. Barnett and K. Xu, *Chem. Rev.*, 2018, **118**, 11433–11456.
4 J. Kasnatscheew, S. Röser, M. Börner and M. Winter, *ACS Appl. Energy Mater.*, 2019, **2**, 7733–7737.
5 M. S. Whittingham, *Chem. Rev.*, 2004, **104**, 4271–4301.
6 P. He, H. J. Yu, D. Li and H. S. Zhou, *J. Mater. Chem.*, 2012, **22**, 3680–3695.
7 B. L. Ellis, K. T. Lee and L. F. Nazar, *Chem. Mater.*, 2010, **22**, 691–714.
8 R. Schmuch, R. Wagner, G. Hörpel, T. Placke and M. Winter, *Nat. Energy*, 2018, **3**, 267–278.
9 J. Kasnatscheew, M. Evertz, B. Streipert, R. Wagner, S. Nowak, I. Cekic Laskovic and M. Winter, *J. Power Sources*, 2017, **359**, 458–467.
10 W. Li, B. Song and A. Manthiram, *Chem. Soc. Rev.*, 2017, **46**, 3006–3059.
11 J. Kasnatscheew, M. Evertz, B. Streipert, R. Wagner, S. Nowak, I. Cekic Laskovic and M. Winter, *J. Phys. Chem. C*, 2017, **121**, 1521–1529.
12 B. Streipert, L. Stolz, G. Homann, P. Janßen, I. Cekic-Laskovic, M. Winter and J. Kasnatscheew, *ChemSusChem*, 2020, **13**, 5301–5307.
13 J. Kasnatscheew, M. Evertz, B. Streipert, R. Wagner, R. Klopsch, B. Vortmann, H. Hahn, S. Nowak, M. Amereller, A. C. Gentschev, P. Lamp and M. Winter, *Phys. Chem. Chem. Phys.*, 2016, **18**, 3956–3965.
14 G. Qian, Y. Zhang, L. Li, R. Zhang, J. Xu, Z. Cheng, S. Xie, H. Wang, Q. Rao, Y. He, Y. Shen, L. Chen, M. Tang and Z.-F. Ma, *Energy Storage Materials*, 2020, **27**, 140–149.
15 W. Li, U.-H. Kim, A. Dolocan, Y.-K. Sun and A. Manthiram, *ACS Nano*, 2017, **11**, 5853–5863.
16 S. M. Bak, E. Y. Hu, Y. N. Zhou, X. Q. Yu, S. D. Senanayake, S. J. Cho, K. B. Kim, K. Y. Chung, X. Q. Yang and K. W. Nam, *ACS Appl. Mater. Interfaces*, 2014, **6**, 22594–22601.
17 L. Wu, K.-W. Nam, X. Wang, Y. Zhou, J.-C. Zheng, X.-Q. Yang and Y. Zhu, *Chem. Mater.*, 2011, **23**, 3953–3960.
18 S. Zhang, J. Ma, Z. Hu, G. Cui and L. Chen, *Chem. Mater.*, 2019, **31**, 6033–6065.
19 M. Evertz, F. Horsthemke, J. Kasnatscheew, M. Börner, M. Winter and S. Nowak, *J. Power Sources*, 2016, **329**, 364–371.

20 P. Niehoff, S. Passerini and M. Winter, *Langmuir*, 2013, **29**, 5806–5816.
21 M. Winter, *Z. Phys. Chem.*, 2009, **223**, 1395–1406.
22 S. Röser, A. Lerchen, L. Ibing, X. Cao, J. Kasnatscheew, F. Glorius, M. Winter and R. Wagner, *Chem. Mater.*, 2017, **29**, 7733–7739.
23 S. Klein, K. Borzutzki, P. Schneider, O. Fromm, J. Reiter, Q. Fan, T. Placke, M. Winter and J. Kasnatscheew, *Chem. Mater.*, 2020, **32**, 6279–6284.
24 J. Kim, H. Ma, H. Cha, H. Lee, J. Sung, M. Seo, P. Oh, M. Park and J. Cho, *Energy Environ. Sci.*, 2018, **11**, 1449–1459.
25 W. Li, *J. Electrochem. Soc.*, 2020, **167**, 090514.
26 O. C. Harris, S. E. Lee, C. Lees and M. Tang, *J. Phys.: Energy*, 2020, **2**, 032002.
27 C. Wang, L. Xing, J. Vatamanu, Z. Chen, G. Lan, W. Li and K. Xu, *Nat. Commun.*, 2019, **10**, 3423.
28 R. Jung, F. Linsenmann, R. Thomas, J. Wandt, S. Solchenbach, F. Maglia, C. Stinner, M. Tromp and H. A. Gasteiger, *J. Electrochem. Soc.*, 2019, **166**, A378–A389.
29 S. Solchenbach, G. Hong, A. T. S. Freiberg, R. Jung and H. A. Gasteiger, *J. Electrochem. Soc.*, 2018, **165**, A3304–A3312.
30 J. A. Gilbert, I. A. Shkrob and D. P. Abraham, *J. Electrochem. Soc.*, 2017, **164**, A389–A399.
31 I. Buchberger, S. Seidlmayer, A. Pokharel, M. Piana, J. Hattendorff, P. Kudejova, R. Gilles and H. A. Gasteiger, *J. Electrochem. Soc.*, 2015, **162**, A2737–A2746.
32 C. Zhan, J. Lu, A. Jeremy Kropf, T. Wu, A. N. Jansen, Y.-K. Sun, X. Qiu and K. Amine, *Nat. Commun.*, 2013, **4**, 2437.
33 S. Klein, P. Bärmann, T. Beuse, K. Borzutzki, J. Frerichs, J. Kasnatscheew, M. Winter and T. Placke, *ChemSusChem*, 2021, **14**, 595–613.
34 X. Fan, G. Hu, B. Zhang, X. Ou, J. Zhang, W. Zhao, H. Jia, L. Zou, P. Li and Y. Yang, *Nano Energy*, 2020, **70**, 104450.
35 W. Li, A. Dolocan, P. Oh, H. Celio, S. Park, J. Cho and A. Manthiram, *Nat. Commun.*, 2017, **8**, 14589.
36 Y. Xia, J. Zheng, C. Wang and M. Gu, *Nano Energy*, 2018, **49**, 434–452.
37 Y. Liu, J. Harlow and J. Dahn, *J. Electrochem. Soc.*, 2020, **167**, 020512.
38 J. Zheng, M. Gu, J. Xiao, P. Zuo, C. Wang and J.-G. Zhang, *Nano Lett.*, 2013, **13**, 3824–3830.
39 D. J. Miller, C. Proff, J. G. Wen, D. P. Abraham and J. Bareño, *Adv. Energy Mater.*, 2013, **3**, 1098–1103.
40 Q. Xia, M. Ni, M. Chen and H. Xia, *J. Mater. Chem. A*, 2019, **7**, 6187–6196.
41 H. Li, J. Li, N. Zaker, N. Zhang, G. A. Botton and J. R. Dahn, *J. Electrochem. Soc.*, 2019, **166**, A1956–A1963.
42 J. Li, H. Li, W. Stone, R. Weber, S. Hy and J. R. Dahn, *J. Electrochem. Soc.*, 2017, **164**, A3529–A3537.
43 J. Li, A. R. Cameron, H. Li, S. Glazier, D. Xiong, M. Chatzidakis, J. Allen, G. A. Botton and J. R. Dahn, *J. Electrochem. Soc.*, 2017, **164**, A1534–A1544.
44 H. Li, J. Li, X. Ma and J. R. Dahn, *J. Electrochem. Soc.*, 2018, **165**, A1038–A1045.
45 X. Fan, Y. Liu, X. Ou, J. Zhang, B. Zhang, D. Wang and G. Hu, *Chem. Eng. J.*, 2020, **393**, 124709.
46 X. Chen, Y. Tang, C. Fan and S. Han, *Electrochim. Acta*, 2020, **341**, 136075.
47 J. Zhu and G. Chen, *J. Mater. Chem. A*, 2019, **7**, 5463–5474.
48 W. H. Kan, D. Chen, J. K. Papp, A. K. Shukla, A. Huq, C. M. Brown, B. D. McCloskey and G. Chen, *Chem. Mater.*, 2018, **30**, 1655–1666.
49 Y. H. Hu, X. H. Zhao and Z. G. Suo, *J. Mater. Res.*, 2010, **25**, 1007–1010.
50 F. Zhang, S. Lou, S. Li, Z. Yu, Q. Liu, A. Dai, C. Cao, M. F. Toney, M. Ge, X. Xiao, W. K. Lee, Y. Yao, J. Deng, T. Liu, Y. Tang, G. Yin, J. Lu, D. Su and J. Wang, *Nat. Commun.*, 2020, **11**, 3050.
51 J. Kim, H. Lee, H. Cha, M. Yoon, M. Park and J. Cho, *Adv. Energy Mater.*, 2018, **8**, 1870023.
52 R. Nölle, K. Beltrop, F. Holtstiege, J. Kasnatscheew, T. Placke and M. Winter, *Mater. Today*, 2020, **32**, 131–146.
53 M. Winter, P. Novak and A. Monnier, *J. Electrochem. Soc.*, 1998, **145**, 428–436.
54 T. Placke, V. Siozios, R. Schmitz, S. F. Lux, P. Bieker, C. Colle, H. W. Meyer, S. Passerini and M. Winter, *J. Power Sources*, 2012, **200**, 83–91.
55 M. Ruttert, V. Siozios, M. Winter and T. Placke, *ACS Appl. Energy Mater.*, 2020, **3**, 743–758.
56 J. Kasnatscheew, M. Evertz, R. Kloepsch, B. Streipert, R. Wagner, I. Cekic Laskovic and M. Winter, *Energy Technol.*, 2017, **5**, 1670–1679.
57 J. Kasnatscheew, U. Rodehorst, B. Streipert, S. Wiemers-Meyer, R. Jakelski, R. Wagner, I. C. Laskovic and M. Winter, *J. Electrochem. Soc.*, 2016, **163**, A2943–A2950.
58 X. Ma, J. E. Harlow, J. Li, L. Ma, D. S. Hall, S. Buteau, M. Genovese, M. Cormier and J. R. Dahn, *J. Electrochem. Soc.*, 2019, **166**, A711–A724.
59 L. Madec, L. Ma, K. J. Nelson, R. Petibon, J.-P. Sun, I. G. Hill and J. R. Dahn, *J. Electrochem. Soc.*, 2016, **163**, A1001–A1009.
60 R. S. Arumugam, L. Ma, J. Li, X. Xia, J. M. Paulsen and J. R. Dahn, *J. Electrochem. Soc.*, 2016, **163**, A2531–A2538.
61 H. Zheng, Q. Sun, G. Liu, X. Song and V. S. Battaglia, *J. Power Sources*, 2012, **207**, 134–140.
62 A. Gupta, E. Kazyak, N. Craig, J. Christensen, N. P. Dasgupta and J. Sakamoto, *J. Electrochem. Soc.*, 2018, **165**, A2801–A2806.
63 G. Homann, L. Stolz, M. Winter and J. Kasnatscheew, *iScience*, 2020, **23**, 101225.
64 G. Homann, L. Stolz, J. Nair, I. C. Laskovic, M. Winter and J. Kasnatscheew, *Sci. Rep.*, 2020, **10**, 4390.
65 G. Bieker, M. Winter and P. Bieker, *Phys. Chem. Chem. Phys.*, 2015, **17**, 8670–8679.
66 G. Homann, L. Stolz, K. Neuhaus, M. Winter and J. Kasnatscheew, *Adv. Funct. Mater.*, 2020, **30**, 2006289.
67 J. Betz, J.-P. Brinkmann, R. Nölle, C. Lürenbaum, M. Kolek, M. C. Stan, M. Winter and T. Placke, *Adv. Energy Mater.*, 2019, **9**, 1900574.